8th International Conference on Multiphase Flow
ICMF 2013, Jeju, Korea, May 26–31, 2013

Droplet Breakup in High-Speed Gas Flows

Jomela C. Meng[1] and Tim Colonius[2]

[1]*Graduate Aerospace Laboratories, California Institute of Technology, Pasadena, CA 91125, U.S.A.*
[2]*Department of Mechanical and Civil Engineering, California Institute of Technology, Pasadena, CA 91125, U.S.A.*

Keywords: breakup, deformation, droplet, shock-cylinder interaction, stripping, unsteady drag coefficient

Abstract

Numerical simulations are performed to study the breakup of water cylinders in the flow behind normal shocks. The computational setup is similar to previous experiments (Igra and Takayama, 2001, 2003). We examine the qualitative features of the so-called stripping breakup observed in the numerical results. Two interesting flow features are discussed: the existence of recirculation regions and an upstream jet in the wake. Various integral quantities associated with the cylinder's deformation and acceleration are computed and compared with the experimental results, with generally good agreement. Furthermore, calculations of the velocity and acceleration of the cylinder's center of mass provide an estimate of the unsteady drag coefficient which is approximately constant over the initial breakup period.

1 Introduction

The study of droplet breakup has important applications in rain erosion damage, combustion and detonation of multiphase mixtures, and the atomization of liquid jets. The primary motivation for the present work resides in geothermal waste heat recovery applications. In order to generate useful power, waste heat energy is transferred to refrigerant through heat exchangers within variable phase turbines (VPTs). Enthalpy is then converted into kinetic energy when the refrigerant is flash evaporated and expanded through a multiphase nozzle. The multiphase mixture at the nozzle exit consists of gaseous refrigerant containing disperse microscopic refrigerant drops that are accelerated by the surrounding flow. From the nozzle, the two-phase jet enters the turbine rotor stage where mechanical work is extracted. From experimental testing, it is known that droplet size has a significant effect on turbine performance. Large droplets tend to form a thin liquid film on the rotor blades that dampens the momentum transfer from droplet impact (Welch and Boyle, 2009). Smaller droplets, on the other hand, still impart momentum during impact, but are more likely to run off the rotor blade with the surrounding gas flow. The evolution of these droplets as they are accelerated through the multiphase nozzle is a complex process due to the multiple physical mechanisms at work. In addition to the phase changes, heat and mass transfer occur at the gas-liquid interface, while Rayleigh-Taylor and Kelvin-Helmholtz instabilities arise on the surface of the droplet. A better understanding of these complicated phenomena and their effects will ultimately allow for optimized multiphase nozzle design.

The annual review by Theofanous (2011) summarizes previous work on the problem of droplet breakup. In a unified fashion, Theofanous discusses the aerobreakup of both Newtonian and viscoelastic liquid drops and provides an overview of the fundamental criticalities in the breakup process. Using the novel approach of laser-induced fluorescence, the experiments of Theofanous et al. (2004) were able to achieve the necessary spatial and temporal resolutions to clearly identify two primary breakup regimes: Rayleigh-Taylor piercing (RTP) and shear-induced entrainment (SIE). The interaction between Kelvin-Helmholtz and Rayleigh-Taylor instabilities are discussed in conjunction with the many competing length and time scales present in the problem.

Historically speaking, most experimental studies of droplet breakup have been conducted in shock tubes where the passage of a normal shock over a droplet provides a step change to uniform flow conditions. One of the earliest examples of this work is the classic paper by Engel (1958) who investigated the breakup of water droplets in the region behind an air shock. Using spark pictures, Engel was able to observe the deformation of the droplet in time and the eventual formation of mist for various droplet sizes ($d_0 = 1.4, 2.7$ mm) and shock strengths ($M_S = 1.3, 1.5, 1.7$). Distortions of the high light in the spark pictures suggested internal changes within the droplet. In addition to mist formation, Engel also observed corrugations and speculated possible causes for radial flow on the surface of the droplet. Utilizing drift measurements taken from the spark pictures, Engel made preliminary attempts to calculate the acceleration and unsteady drag coefficient of the water drops. The analysis concluded that the unsteady drag coefficient of the deforming drops compared well with that of a perforated disk.

The computational costs of full three-dimensional simulations of the breakup of spherical droplets are often too prohibitive to allow comparisons with experiments. To circumvent this problem, breakup is often studied using two-dimensional simulations which are physically equivalent to the breakup of liquid columns or cylinders. The work of Igra and Takayama (2001, 2003) provides useful validation since their experiments investigated the breakup of water cylinders in the flow behind a shock wave. Using holographic

interferometry for visualization, they were able to measure drift and quantify deformation of the water cylinders. The temporal evolution of the cylinder's trajectory allowed Igra and Takayama to reconstruct the cylinder's velocity and acceleration. An unsteady drag coefficient for the deforming cylinder was computed assuming constant cylinder acceleration.

The goals of the present work are to provide insight into the physics of breakup through numerical simulations. To that end, the physical model and relevant simulation parameters are presented in Section 2. Section 3 describes and validates the employed numerical method. Computational results and a discussion of their implications follow in Section 4. Finally, Section 5 summarizes the conclusions.

Nomenclature

a	Acceleration vector, $(a_x, a_y)^T$
I	Identity matrix
u	Velocity vector, $(u, v)^T$
x	Position vector, $(x, y)^T$
A	Area [m^2]
c	Sound speed [m/s]
C_D	Drag coefficient
D	Drag force [N]
d	Cylinder diameter [m]
E	Total energy [J]
k	Numerical schlieren scaling parameter
M	Mach number
m	Mass [kg]
p	Pressure [Pa]
P_∞	Stiffness constant [Pa]
Re	Reynolds number
S	Frontal area [m]
t	Time [s]
w	Centerline width [m]
We	Weber number

Greek Letters

α	Volume fraction
β	Linear Hugoniot slope coefficient
γ	Ratio of specific heats
μ	Dynamic viscosity [Pa·s]
ϕ	Numerical schlieren function
ρ	Density [kg/m^3]
σ	Surface tension coefficient [N/m]

Superscripts

$\bar{}$	Center of mass
*	Non-dimensionalized

Subscripts

0	Initial/Nominal
1	Pre-shock
2	Post-shock
G	Gas
L	Liquid
P	Particle
S	Shock

2 Physical model

2.1 Problem description

The problem of droplet breakup is studied in two dimensions by simulating the breakup of a water cylinder in the high-speed flow behind a normal shock wave. The experiments of Igra and Takayama (2001, 2003) are replicated by simulating the passages of Mach 1.18, 1.47, and 1.73 shock waves over a 4.8 mm diameter cylinder and a Mach 1.30 shock over a 6.4 mm diameter cylinder. Within the literature, the Weber and Reynolds numbers have, respectively, been used to characterize the relative importance of inertial-to-capillary and inertial-to-viscous forces. The Weber number is typically taken to be

$$We = \frac{\rho_G u_G^2 d_0}{\sigma} \tag{1}$$

where the density and velocity are those of the shocked gas, and the characteristic length scale is the initial cylinder/droplet diameter. Using the experimental parameters for a water droplet in air, and a surface tension coefficient of $\sigma = 0.07286$ N/m, the approximate Weber numbers corresponding to Mach 1.18, 1.30, 1.47, and 1.73 shock waves are, respectively, 940, 3,700, 7,300, and 19,300. These high Weber numbers suggest that the physical mechanisms of breakup are inertially driven, and that in the early stages, the neglect of surface tension is acceptable. The Reynolds number is typically taken as

$$Re = \frac{\rho_G u_G d_0}{\mu_G} \tag{2}$$

where the density, velocity, and dynamic viscosity are, again, those of the shocked gas, and the characteristic length scale is the original cylinder/droplet diameter. Taking the dynamic viscosity of air to be $\mu = 1.8 \times 10^{-5}$ Pa·s, the approximate Reynolds numbers corresponding to the four shock strengths are, respectively, 39,900, 98,600, 131,400, and 237,600. These large Reynolds numbers indicate that, in addition to surface tension, the effects of viscosity can also be ignored for the early stages of breakup.

The breakup of the water cylinder is simulated using the computational setup shown in Figure 1.

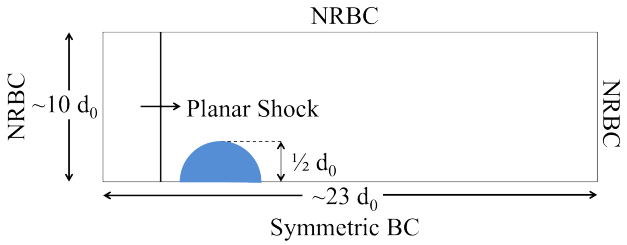

Figure 1: Computational domain setup

For early times, the flow is assumed to be top-bottom symmetric and only half of the water cylinder is simulated. A symmetric boundary condition is applied along the bottom of the domain and non-reflecting boundary conditions

(NRBC) are enforced on the other three sides. To avoid a discontinuous interface in the initial condition, the cylindrical geometry is smoothed onto the Cartesian grid using an initial smoothing function. The water cylinder and the air in front of the planar shock are initially at rest ($\rho_G = 1.401\,\text{kg/m}^3$, $\rho_L = 1000\,\text{kg/m}^3$, and $p_G = p_L = 1\,\text{atm}$). At the start of the simulation, the shock is set in motion towards the water cylinder and establishes a steady freestream flow field.

2.2 Equations of motion

In the absence of surface tension and viscosity (which are justified in Section 2.1) the flow is governed by the multicomponent, compressible Euler equations. Multicomponent flows consist of immiscible fluids that do not change phase. Each fluid (both air and water) is considered to be inviscid and compressible. Material interfaces, in the absence of mass transfer and surface tension, are simply advected by the local velocity field. Following the five-equation model of Allaire et al. (2002), interfaces are modeled using volume fractions. The governing equations are shown below and consist of two continuity equations (3)–(4), one mixture momentum equation (5), one mixture energy equation (6), and one volume fraction advection equation (7).

$$\frac{\partial \alpha_G \rho_G}{\partial t} + \nabla \cdot (\alpha_G \rho_G \mathbf{u}) = 0 \tag{3}$$

$$\frac{\partial \alpha_L \rho_L}{\partial t} + \nabla \cdot (\alpha_L \rho_L \mathbf{u}) = 0 \tag{4}$$

$$\frac{\partial \rho \mathbf{u}}{\partial t} + \nabla \cdot (\rho \mathbf{u} \otimes \mathbf{u} + p\mathbf{I}) = \mathbf{0} \tag{5}$$

$$\frac{\partial E}{\partial t} + \nabla \cdot [(E+p)\mathbf{u}] = 0 \tag{6}$$

$$\frac{\partial \alpha_G}{\partial t} + \mathbf{u} \cdot \nabla \alpha_G = 0 \tag{7}$$

Since a continuity equation is solved for each of the fluids, individual mass (and therefore, total mass) is conserved. Due to the employed numerical method, interfaces are diffuse (smeared over several grid cells) and a smooth transition exists between the two fluids. In what follows, we define a threshold volume fraction that determines a nominal sharp interface location.

All physical flow variables in the solver are non-dimensionalized by the original cylinder diameter, and the nominal density and sound speed of water ($c_L = 1450\,\text{m/s}$). An appropriate time scaling characteristic of drop breakup by Rayleigh-Taylor or Kelvin-Helmholtz instabilities can be found in the literature (Ranger and Nicholls, 1968, Simpkins and Bales, 1972, Pilch and Erdman, 1987). The resultant non-dimensional time is reproduced in (8), and has been used to successfully scale the breakup process across a wide range of conditions.

$$t^* = t \frac{u_G}{d_0} \sqrt{\frac{\rho_G}{\rho_L}} \tag{8}$$

where the density ratio refers to post-shock conditions. Following the analysis of Igra and Takayama (2001, 2003), a slightly different time scaling is used in the present work which does not include the gas-to-liquid density ratio. Therefore, the characteristic breakup time shown in the present work is defined as

$$t^* = t \frac{u_G}{d_0} \tag{9}$$

2.3 Equation of state

The stiffened gas equation of state (Harlow and Amsden, 1971) is used to close the system of equations and models both gases and liquids in the flow solver.

$$\Gamma p + \Pi_\infty = E - \frac{1}{2}\rho \mathbf{u} \cdot \mathbf{u} \tag{10}$$

where

$$\Gamma = \frac{1}{\gamma - 1} = \sum_{i=1}^{2} \alpha_i \left(\frac{1}{\gamma_i - 1} \right) \tag{11}$$

$$\Pi_\infty = \frac{\gamma P_\infty}{\gamma - 1} = \sum_{i=1}^{2} \alpha_i \left(\frac{\gamma_i P_{\infty,i}}{\gamma_i - 1} \right) \tag{12}$$

are the mixture properties in the diffuse interface region (Allaire et al., 2002). For air, $\gamma = 1.401$ is the ratio of specific heats, $P_\infty = 0$, and the stiffened gas equation of state reduces to the ideal gas equation. The parameters γ and P_∞ for water are empirically determined from shock-Hugoniot data (Marsh, 1980) according to the methodology of Johnsen (2007). If $\beta = \frac{\partial U_S}{\partial U_P}$ is the linear Hugoniot slope coefficient, then γ and P_∞ are given by (13) and (14) where the subscript 0 represents the nominal value at STP.

$$\gamma = 2\beta\big(1 + \frac{1}{M_S}\big) - 1 \tag{13}$$

$$P_\infty = \frac{\rho_0 c_0^2}{\gamma} - p_0 \tag{14}$$

These parameters, along with the post-shock conditions in air for the shock-moving reference frame, are tabulated in Table 1.

		Air		Water	
M_S	M_2	ρ [kg/m^3]	p [MPa]	γ	P_∞ [GPa]
1.18	0.26	1.574	0.148	5.577	0.377
1.30	0.41	1.825	0.183	5.298	0.397
1.47	0.58	2.181	0.239	4.982	0.422
1.73	0.79	2.706	0.337	4.618	0.455

Table 1: Post-shock conditions in air and stiffened gas equation of state parameters for water

3 Numerical method

3.1 Spatial and temporal discretization

The current numerical method is based on the work of Johnsen and Colonius (2006) and was shown to be both interface- and shock-capturing. The original numerical scheme was used to investigate the collapse of an air bubble near a rigid wall (Johnsen and Colonius, 2009). A three-dimensional extension of Johnsen's method, including an improved spatial reconstruction approach, has successfully modeled the shock-induced collapse of bubbles (Coralic and Colonius, 2012). The numerical method is based on a finite-volume framework. Spatial reconstruction is accomplished with a third-order weighted essentially non-oscillatory scheme used in conjunction with the Harten-Lax-van Leer-Contact approximate Riemann solver. An explicit third-order total variation diminishing Runge-Kutta scheme is used to march the equations forward in time. A Cartesian grid of 1200x600 cells is stretched near the boundaries by a smooth hyperbolic tangent function. The most refined portion of the grid is located around the initial position of the cylinder and in the region of the near-field wake. In this region, the nominal grid resolution is 100 cells per cylinder diameter. Since the time scheme is explicit, the time-step is chosen to limit the Courant-Friedrichs-Lewy (CFL) stability criterion to CFL ≈ 0.25. For purposes of brevity, verification and validation test cases are not shown for the flow solver. However, standard benchmark tests (e.g. isolated interface advection, Sod's shock tube, liquid-gas Riemann problem, and strong shock in gases) have been satisfactorily completed and will be shown in a future publication.

3.2 Boundary conditions

Non-reflecting boundary conditions are implemented by extrapolating the Riemann state at the edge of the domain. In order to avoid using stencil points outside the computational domain, the order of the WENO scheme is gradually reduced as the boundary is approached. As implemented, the Riemann boundary condition does not contaminate the solution through the reflection of outgoing waves.

3.3 Numerical viscosity

As a consequence of the employed numerical scheme, numerical viscosity is present in the simulation. Based on preliminary viscous simulations, the *effective* Reynolds number associated with this numerical viscosity is believed to be no less than 500 at the level of resolution used in the present results. This corresponds to a physical droplet with a diameter of approximately 15 μm. Further details of the viscous simulations will be presented in forthcoming publications. Without the presence of physical viscosity to regularize the smallest scales, ever finer flow features are resolved in the simulation as spatial resolution is improved. Therefore, traditional grid convergence or independence of the computational results cannot be definitively shown; this is a known issue associated with "inviscid" calculations using shock- and interface-capturing methods. We believe that the present spatial resolution is able to capture the salient features in the flow without being computationally cumbersome.

3.4 Numerical schlieren function

Visualization of the temporal evolution of the flow field around the water cylinder is achieved using a numerical schlieren function originally derived by Quirk and Karni (1996). This schlieren function is computed as the exponential of the negative, normalized density gradient

$$\phi = \exp\left(- k \frac{|\nabla \rho|}{\max|\nabla \rho|} \right) \tag{15}$$

where k is a scaling parameter that allows simultaneous visualization of waves in both fluids. Following Johnsen (2007), $k = 40$ for air and $k = 400$ for water.

3.5 Center of mass calculations

Analysis of the cylinder's drift and unsteady acceleration requires computing the position, velocity, and acceleration of the cylinder's center of mass (COM). The location of the COM is expressed as

$$\bar{\mathbf{x}} = \frac{\int \alpha_L \rho_L \mathbf{x} dA}{\int \alpha_L \rho_L dA} \tag{16}$$

Similarly, the COM's velocity and acceleration can be calculated as

$$\bar{\mathbf{u}} = \frac{\int \alpha_L \rho_L \mathbf{u} dA}{\int \alpha_L \rho_L dA} \tag{17}$$

$$\bar{\mathbf{a}} = \frac{\int \alpha_L \rho_L \mathbf{a} dA}{\int \alpha_L \rho_L dA} \tag{18}$$

provided there is no flux of liquid mass across the domain boundaries. As long as the liquid mass flux is zero, (16)–(18) can be computed by a discrete integration over the entire computational domain. Once liquid mass is lost through the boundaries, (17) and (18) can no longer be used, and the analysis is terminated.

4 Results and discussion

4.1 Breakup regimes

Historically, the Weber number has been used to characterize the various breakup regimes. Much of the earlier literature separates breakup into five distinct regimes: vibrational, bag, bag-and-stamen, shear or sheet stripping, and catastrophic. Detailed descriptions of each breakup regime and the approximate Weber number ranges in which they are applicable can be found in Pilch and Erdman (1987) and Theofanous et al. (2004). More recently, the work of Theofanous et al. (2004) and Theofanous and Li (2008) argues for a re-classification into the two main regimes of RTP and SIE. Theofanous and Li (2008) asserts that catastrophic

breakup was a mirage of low-resolution shadowgraph visualizations and that, instead, SIE is the terminal regime. The SIE regime is thought to be asymptotic for $We > 10^3$. The relevant Weber numbers for the simulated conditions (calculated in Section 2.1) predict that the water cylinders will break up via a stripping mechanism.

4.2 Qualitative features of breakup

For all four investigated shock strengths, the qualitative flow features of the breakup process remain similar with differences arising only when quantifying length and time scales. In this section, we will focus solely on the Mach 1.47 case. A time history of the breakup process is shown in Figure 2. The actual passage of the normal shock over the cylinder does little in terms of cylinder deformation. Instead, the normal shock serves as a consistent and repeatable way to set up a step change to uniform flow conditions around the cylinder. This has been noted before in the literature and is attributed to the fact that the time scale of the discontinuous shock is much smaller than the relaxation time of the cylinder (Aalburg et al., 2003). In fact, for the very early stages of breakup, the water cylinder can be approximated as a solid cylinder. The original shock and reflected wave are seen in Figure 2(b). Behind the reflected wave is a high pressure region associated with the forward flow stagnation point. At a point on the surface preceding the equator of the cylinder, the wall inclination angle decreases beyond a critical angle and the regular reflection transitions into a Mach reflection shown in Figure 2(c). This transition marks the peak drag experienced by the water cylinder. A more detailed explanation of this phenomenon (as it applies to solid cylinders and spheres) can be found in Takayama and Itoh (1986) and Tanno et al. (2003). The convergence of the Mach stems results in the formation of a secondary wave system (Figure 2(d)) that generates high pressures at the rear stagnation point. The non-uniform pressure field around the cylinder causes an initial flattening that is reinforced by the pulling of material at the equator by the surrounding high-speed flow. Joseph et al. (1999) suggests that the early time flattening is independent of viscosity or material type at large Weber number. In conjunction with the lateral elongation, tips are observed to form at the cylinder's periphery (Figure 2(e–f)) and are thought to be the beginning of the stripping process (Chen, 2008). Over time, these tips are drawn downstream and thin filaments of liquid are stripped off the cylinder (Figure 2(j)). Although not captured in these simulations (due to the neglect of surface tension) the rise of capillary instabilities cause the filaments to disintegrate downstream of the original cylinder. The formation of a complex wake behind the deforming cylinder is driven by unsteady vortex shedding. The wake is initially comprised of a single large vortex seen in Figure 2(d–f). This vortex entrains downstream fluid and jets it upstream to impinge on the back of the cylinder. The presence of a standing shock in the wake (visible in Figure 2 (e–g)) is associated with the turning of the locally supersonic flow. As more vortices are shed, the wake becomes increasingly chaotic (Figure 2(g–j)). It is interesting to note that the presence of an upstream jet along the centerline persists for the duration of the simulation.

From Figure 2, there are two interesting flow features that arise in the simulation that deserve further discussion. First is the existence of recirculation regions near the equator of the deforming cylinder (visible in Figure 2(f–m)). Consider, for now, the top half of the water cylinder.

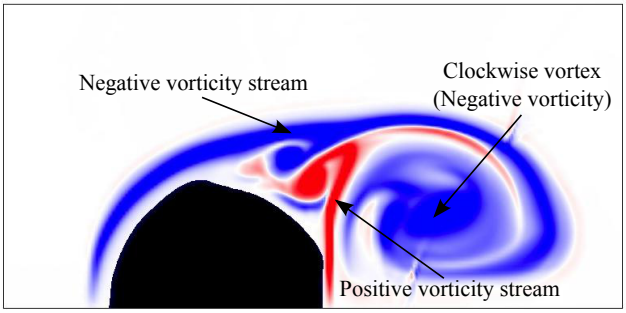

Figure 3: Positive (*red*) and negative (*blue*) vorticity streams at $t^* = 3.67$

As the normal shock traverses the hemisphere, the baroclinic contribution to vorticity, $\frac{1}{\rho^2}\nabla\rho\times\nabla p$, generates negative vorticity along the surface which is transported downstream by the surrounding flow. This stream of negative vorticity is the source of vortex shedding that creates the wake behind the deforming cylinder. Shortly after the shockwave has completed its pass, strong positive vorticity is generated, again by the baroclinic term, at the back of the cylinder. The large stationary (clockwise) vortex in the cylinder's wake advects this stream of positive vorticity up along the flattened back of the cylinder until it runs perpendicularly into the stream of negative vorticity coming off the front of the cylinder. These two streams of opposite vorticity interact to form a recirculation region comprised of two counter-rotating vortices that are trapped by the two streams and the cylinder itself (see Figure 3). This recirculation region remains for a significant time period and appears to contribute to the stripping action at the edge of the cylinder. In time, as the cylinder is flattened by pressure forces, the recirculation region is compressed in the flow direction. Eventually, the two streams of opposite vorticity are bent in parallel with the flow and the recirculation region disappears.

The second interesting feature observed in the numerical simulations is the presence of an upstream jet in the wake behind the cylinder. As mentioned previously, this upstream jet persists for the entirety of the numerical simulation. One possible explanation is that the jet is an artifact of assuming symmetry in the simulation. It is well known that for a large range of Reynolds numbers ($45 < Re < 10^5$), flow around a rigid cylinder will generate a von Kármán vortex street. Note that the symmetry assumption is acceptable for the early stages of breakup since a finite time is required to establish the vortex street. For the Reynolds numbers corresponding to the simulations, it is entirely conceivable that a vortex street might develop in the wake of the deforming water cylinder. If, indeed, a vortex street is established, it is possible that the upstream jet will decrease in strength or

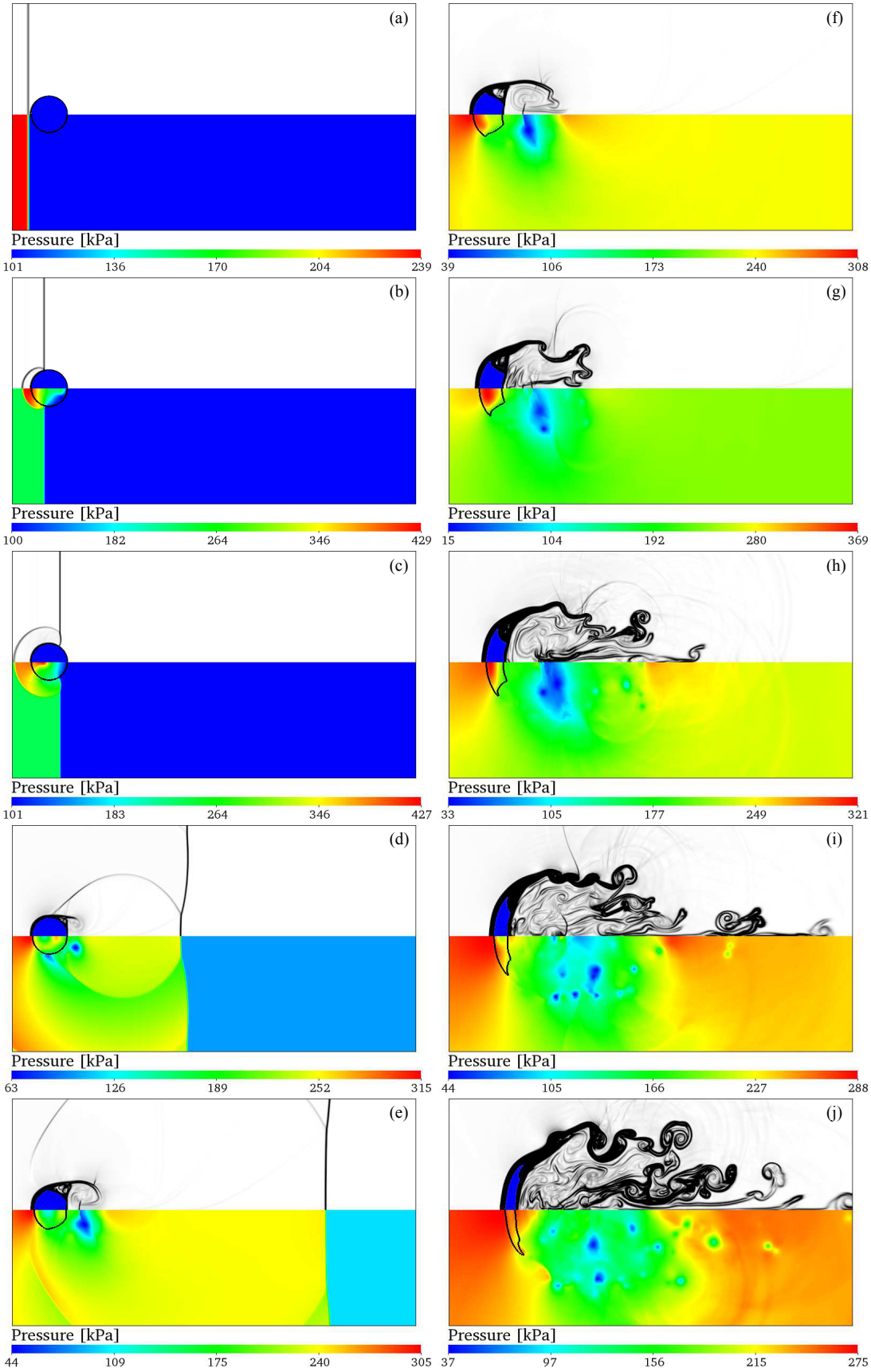

Figure 2: Numerical schlieren images (*top*) and filled pressure contours (*bottom*) of the breakup of a 4.8 mm cylinder at $t^* =$ (a) 0.00 (b) 0.17 (c) 0.36 (d) 1.92 (e) 3.67 (f) 5.62 (g) 9.51 (h) 13.41 (i) 17.31 (j) 22.18 behind a Mach 1.47 shockwave (*top to bottom, left to right*). Isocontours are shown for $\alpha_L \geq 0.9$.

cease to exist altogether. One final point to mention is that the strength/existence of the upstream jet may also change for three-dimensional simulations of a spherical droplet due to the "flow-relieving effect" of the third dimension.

4.3 Deformation

To quantify the deformation of the water cylinders in time, Igra and Takayama (2001, 2003) measured the deformed diameter, centerline width, and coherent body area from holographic interferograms. In the following plots, the experimental data of Igra and Takayama (2001, 2003) are shown as discrete points, and the results of the simulations are represented by curves. The time evolution of the non-dimensionalized cylinder diameters are shown in Figure 4.

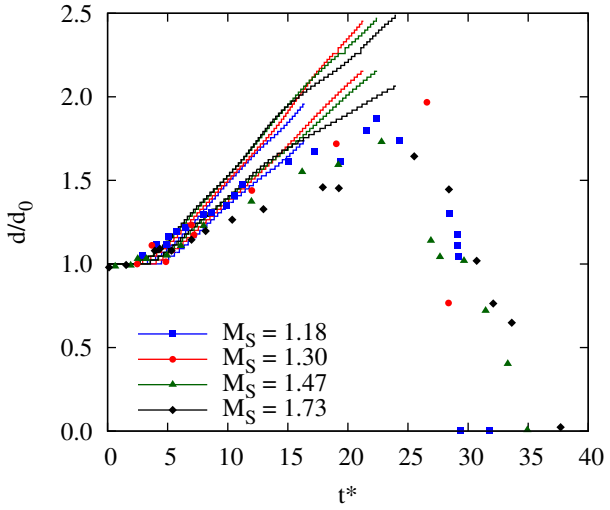

Figure 4: Deformed diameter of the water cylinder

The stepped nature of the curves is an artifact of using the nearest grid cell to the threshold volume fraction criterion. From their discussion, it was not possible to unambiguously identify the criteria Igra and Takayama (2001, 2003) used to determine the boundaries of the deforming body. The issue is confounded in our situation since the interface is diffuse at finite resolution. Therefore, instead of specifying a single value of the threshold volume fraction, an appropriate range is chosen in an attempt to bound the experimental data. For each shock Mach number (differentiated by color), there are two distinct curves representing the bounds of the specified threshold volume fraction range. The upper curves and lower curves in Figure 4 correspond, respectively, to threshold volume fractions of $\alpha_L = 0.9$ and $\alpha_L = 0.99$. Lowering the threshold volume fraction to a value less than 0.9 has the effect of shifting the curves even higher. From the experimental data, it can be seen that the cylinder diameter initially grows in time as the cylinder is compressed in the flow direction and laterally stretched. At a critical maximum value, however, the diameter stops increasing and begins to decrease as material is continually stripped off the edge.

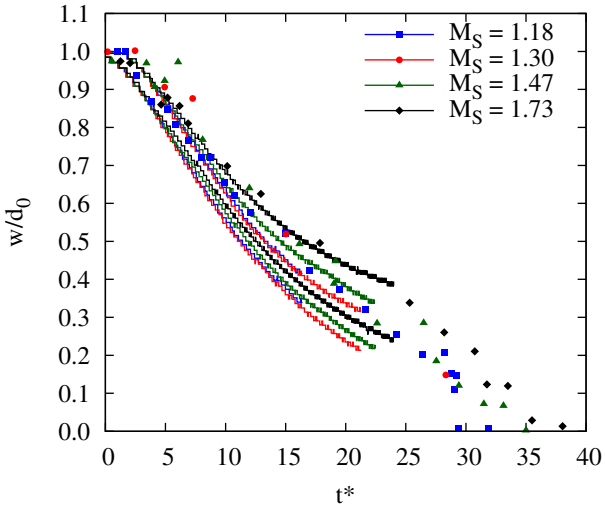

Figure 5: Centerline dimension of the water cylinder

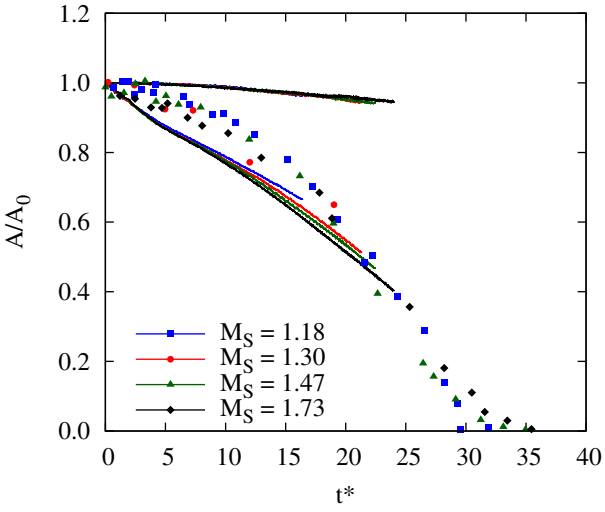

Figure 6: Area of the coherent cylinder body

Numerical measurements of the cylinder's centerline width and coherent body area in Figures 5 and 6 compare well to the experimental data for a threshold volume fraction range between $0.5 < \alpha_L < 0.99$. The streamwise centerline dimension of the cylinders monotically decreases due to compression until all the material has been stripped from the periphery and the cylinder no longer exists. This idea of constant stripping of material from the coherent body is reinforced by the persistent loss of body area.

4.4 Drift, velocity, and acceleration

From the holographic interferograms, Igra and Takayama (2001, 2003) were able to measure the drift of the cylinders as a function of time. Their measurements were based on the location of the cylinder's front. In Figure 7, the numerical measurements of drift are plotted against the experimental data and are color coded by shock Mach number.

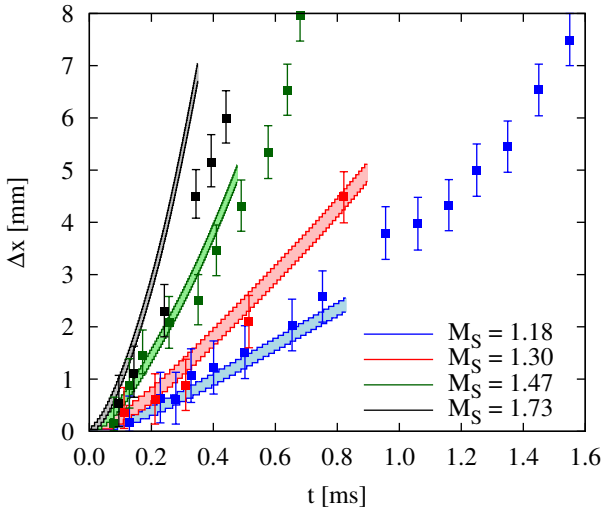

Figure 7: Drift of the water cylinder

It is clear that as shock strength is increased, the water cylinder experiences greater accelerations. This is expected considering the fact that, in the shock-moving reference frame, post-shock air velocity increases with shock Mach number. Reasonable agreement is found for early times and numerical results are within experimental error for the weaker shocks. For reasons we do not yet understand, the comparison appears to deteriorate with increasing shock strength. The measurement of drift from the forward stagnation point is a necessary simplification for extracting meaningful data from photographic evidence, and has been used in other work (e.g. Engel (1958), Simpkins and Bales (1972)). However, as noted in Theofanous (2011), the drift of the front of the cylinder is not an accurate representation of the drift of the cylinder's COM. In fact, the drift computed from the front tends to overestimate, and then underestimate the true drift of the COM.

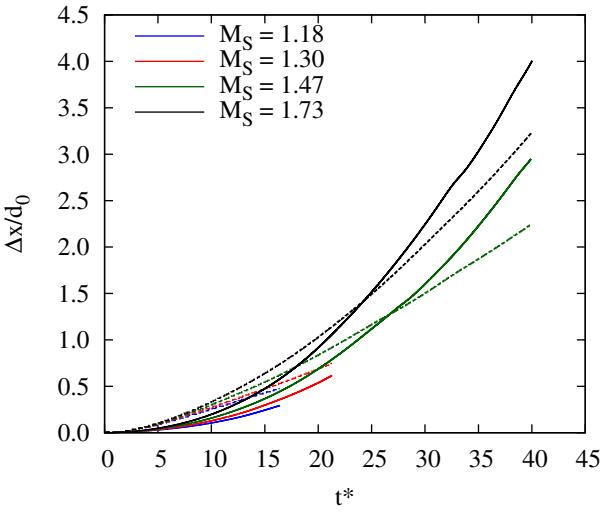

Figure 8: Drift of the water cylinder as measured from the COM (*solid*) and forward stagnation point (*dashed*)

This is clearly seen in Figure 8 which shows the streamwise location of the COM in comparison with the location of the cylinder front. Note that the curves for the Mach 1.47 and 1.73 shocks have not been terminated to show both the over- and under-estimation. Though both measurements of drift exhibit similar behavior, an accurate calculation of the cylinder's acceleration and drag must be based on the cylinder's COM. The smooth, parabolic nature of the drift curves has led previous work to assume that the cylinder undergoes a constant acceleration.

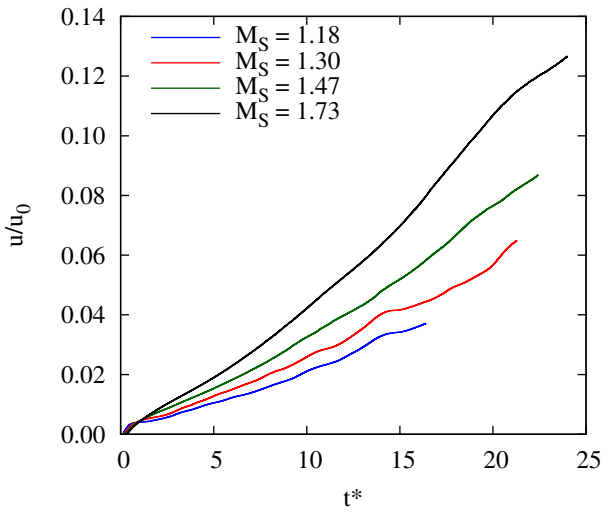

Figure 9: Velocity of the water cylinder

Using (17), the streamwise velocity of the cylinder is plotted in Figure 9 for the four shock Mach numbers. These curves deviate from the straight velocity lines expected for the case of constant acceleration.

In fact, the COM acceleration in the streamwise direction, calculated using (18), shows significant oscillations.

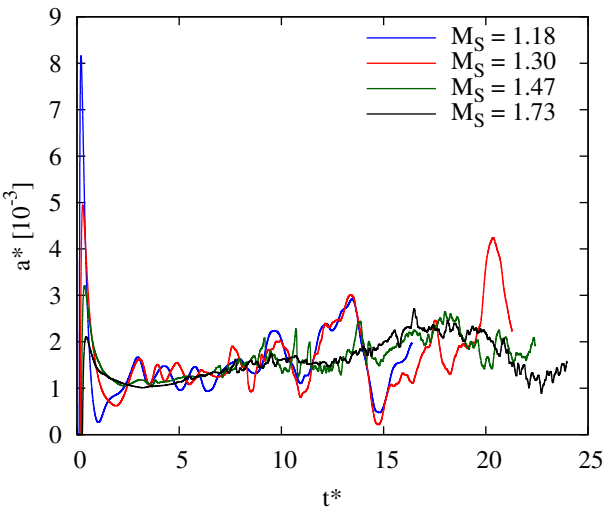

Figure 10: Acceleration of the water cylinder

In Figure 10, the acceleration has been non-dimensionalized as

$$a^* = a\left(\frac{d_0}{u_G^2}\right)\left(\frac{p_1}{p_2}\right) \tag{19}$$

Scaling by the pressure ratio across the shock appears to collapse the transient acceleration behavior. The initial spike in acceleration is, of course, the passage of the shock wave over the cylinder. The maximum peak occurs when the shock reflection transitions from a regular reflection to a Mach reflection. Once the shock has passed, the surrounding high-speed gas begins to accelerate the cylinder. The frequency and amplitude of the oscillations seem to increase and decrease, respectively, with increasing shock strength. We believe that these oscillations are related to the vortex shedding process. For the same characteristic breakup time, the wakes for the stronger shock cases are more developed than those of the weaker shocks and are comprised of a greater number of shed vortices. Though further investigation into this phenomenon is required, it seems plausible that the difference in wake development could lead to the changes in oscillation frequency and amplitude.

With the knowledge of all the relevant flow variables, an attempt can be made to calculate the unsteady drag coefficient of the deforming cylinder. The drag coefficient is defined as

$$C_D = \frac{D}{\frac{1}{2}\rho u^2 S} = \frac{ma}{\frac{1}{2}\rho_G (u_G - u)^2 d} \tag{20}$$

The velocity and acceleration of the cylinder are known, the mass, gas density, and post-shock air velocity are constants, and d is the deformed diameter of the cylinder. Using (20), the unsteady drag coefficients for different shock strengths collapse to a relatively steady value for a significant period of time.

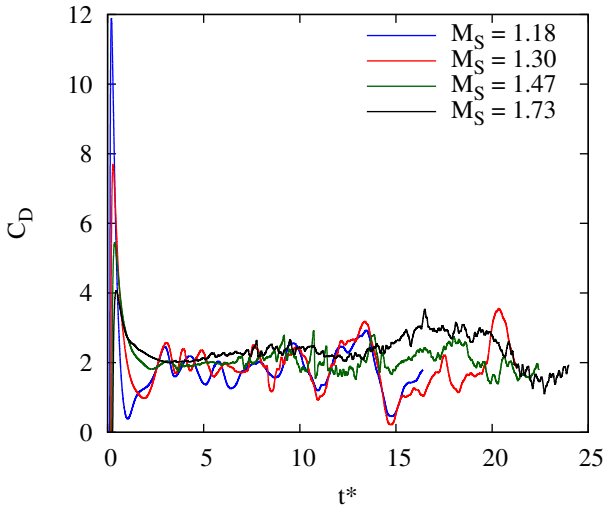

Figure 11: Unsteady drag coefficient of the water cylinder

Oscillations are still present, but fluctuate around a mean value. The deformed diameter used in the drag coefficient calculation is based on a threshold volume fraction of $\alpha_L = 0.99$. Lowering the threshold volume fraction does not significantly alter the drag coefficient curves. It has been tested and confirmed that the stairstep nature of the diameter curve does not introduce significant noise into the drag coefficient calculation.

5 Conclusions

In conclusion, simulations of the breakup of water cylinders in the flow behind normal shock waves were performed and compared to published experimental data. The numerical results support previous experimental observations regarding the stripping breakup of the water cylinder. Recirculation regions near the equator of the deforming cylinder were found to be the result of the interaction of two streams of opposite vorticity. An upstream jet was also observed in the wake of the deforming cylinder which persisted for long times. Measurements of the cylinder's drift and various benchmarks of deformation showed reasonable agreement with those from the experiments. A characteristic breakup time found within the literature successfully scaled time across the four investigated shock strengths. Finally, calculations of velocity and acceleration from the cylinder's center of mass exhibited deviations from constant acceleration. Using the deformed diameter, and the actual velocity and acceleration, an unsteady drag coefficient was computed which showed collapse and fluctuated about a relatively steady mean value. The move to full three-dimensional simulations and the implementation of surface tension will facilitate comparisons with droplet experiments and allow the simulations to capture even more of the complicated flow physics present in the breakup process.

Acknowledgments

We are grateful to Vedran Coralic who developed the flow solver and graciously shared the source code with us. Also, thanks to Guillaume Blanquart for his insight and guidance in many useful discussions.

References

C. Aalburg, B. Van Leer, and G. M. Faeth. Deformation and drag properties of round drops subjected to shock-wave disturbances. *AIAA J.*, 41(12):2371–2378, 2003.

G. Allaire, S. Clerc, and S. Kokh. A five-equation model for the simulation of interfaces between compressible fluids. *J. Comput. Phys.*, 181:577–616, 2002.

H. Chen. Two-dimensional simulation of stripping breakup of a water droplet. *AIAA J.*, 46(5):1135–1143, 2008.

V. Coralic and T. Colonius. Shock-induced collapse of a bubble inside a deformable vessel. *Eur. J. Mech. B-Fluid*, In Press, 2012.

O. G. Engel. Fragmentation of waterdrops in the zone behind an air shock. *J. Res. Nat. Bur. Stand.*, 60(3):245–280, March 1958.

F. H. Harlow and A. A. Amsden. Fluid dynamics. Technical Report LA-4700, LASL, June 1971.

D. Igra and K. Takayama. A study of shock wave loading on a cylindrical water column. Technical Report Vol. 13, pp. 19–36, Institute of Fluid Science, Tohoku University, March 2001.

D. Igra and K. Takayama. Experimental investigation of two cylindrical water columns subjected to planar shock wave loading. *J. Fluid Eng. - T. ASME*, 125:325–331, 2003.

E. Johnsen. *Numerical simulations of non-spherical bubble collapse with applications to shockwave lithotripsy*. PhD thesis, California Institute of Technology, Pasadena, CA, 2007.

E. Johnsen and T. Colonius. Implementation of WENO schemes in compressible multicomponent flow problems. *J. Comput. Phys.*, 219:715–732, December 2006.

E. Johnsen and T. Colonius. Numerical simulations of non-spherical bubble collapse. *J. Fluid Mech.*, 629:231–262, 2009.

D. D. Joseph, J. Belanger, and G. S. Beavers. Breakup of a liquid drop suddenly exposed to a high-speed airstream. *Int. J. Multiphase Flow*, 25:1263–1303, 1999.

S. P. Marsh, editor. *LASL Shock Hugoniot Data*. University of California Press, 1980.

M. Pilch and C. A. Erdman. Use of breakup time data and velocity history data to predict the maximum size of stable fragments for acceleration-induced breakup of a liquid drop. *Int. J. Multiphase Flow*, 13(6):741–757, 1987.

J. J. Quirk and S. Karni. On the dynamics of a shock-bubble interaction. *J. Fluid Mech.*, 318:129–163, 1996.

A. A. Ranger and J. A. Nicholls. Aerodynamic shattering of liquid drops. *AIAA J.*, (68-83), 1968.

P. G. Simpkins and E. L. Bales. Water-drop response to sudden accelerations. *J. Fluid Mech.*, 55:629–639, 1972.

K. Takayama and K. Itoh. Unsteady drag over cylinders and aerofoils in transonic shock tube flows. Technical Report Vol. 51, Institute of High Speed Mechanics, Tohoku University, Sendai, Japan, 1986.

H. Tanno, K. Itoh, T. Saito, A. Abe, and K. Takayama. Interaction of a shock with a sphere suspended in a vertical shock tube. *Shock Waves*, 13:191–200, 2003.

T. G. Theofanous. Aerobreakup of Newtonian and viscoelastic liquids. *Annu. Rev. Fluid Mech.*, 43:661–690, 2011.

T. G. Theofanous and G. J. Li. On the physics of aerobreakup. *Phys. Fluids*, 20(052103), 2008.

T. G. Theofanous, G. J. Li, and T. N. Dinh. Aerobreakup in rarefied supersonic gas flows. *J. Fluid Eng. - T. ASME*, 126:516–527, 2004.

P. Welch and P. Boyle. New turbines to enable efficient geothermal power plants. In *GRC Transactions*, volume 33, pages 765–772, 2009.